FOCUS ISSUE OF SELECTED PAPERS FROM IMLB 2016 WITH INVITED PAPERS CELEBRATING 25 YEARS OF LITHIUM ION BATTERIES

Garnet-Type $Li_7La_3Zr_2O_{12}$ Solid Electrolyte Thin Films Grown by CO_2-Laser Assisted CVD for All-Solid-State Batteries

Christoph Loho,[a,z] Ruzica Djenadic,[a,b] Michael Bruns,[c] Oliver Clemens,[a,d] and Horst Hahn[a,b,d]

[a]*Joint Research Laboratory Nanomaterials, Technische Universität Darmstadt and Karlsruhe Institute of Technology, 64287 Darmstadt, Germany*
[b]*Electrochemical Energy Storage, Helmholtz Institute Ulm, 89081 Ulm, Germany*
[c]*Institute for Applied Materials and Karlsruhe Nano Micro Facility, Karlsruhe Institute of Technology, 76344 Eggenstein-Leopoldshafen, Germany*
[d]*Institute of Nanotechnology, Karlsruhe Institute of Technology, 76344 Eggenstein-Leopoldshafen, Germany*

The detailed characterization of garnet-type Li-ion conducting $Li_7La_3Zr_2O_{12}$ (LLZO) solid electrolyte thin films grown by novel CO_2-laser assisted chemical vapor deposition (LA-CVD) is reported. A deposition process parameter study reveals that an optimal combination of deposition temperature and oxygen partial pressure is essential to obtain high quality tetragonal LLZO thin films. The polycrystalline tetragonal LLZO films grown on platinum have a dense and homogeneous microstructure and are free of cracks. A total lithium ion conductivity of $4.2 \cdot 10^{-6}$ S · cm^{-1} at room temperature, with an activation energy of 0.50 eV, is achieved. This is the highest total lithium ion conductivity value reported for tetragonal LLZO thin films so far, being about one order of magnitude higher than previously reported values for tetragonal LLZO thin films prepared by sputtering and pulsed laser deposition. The results of this study suggest that the tetragonal LLZO thin films grown by LA-CVD are applicable for the use in all-solid-state thin film lithium ion batteries.

Manuscript submitted September 26, 2016; revised manuscript received November 8, 2016. Published November 22, 2016. This was Paper 718 presented at the Chicago, Illinois, Meeting of the IMLB, June 19–24, 2016. *This paper is part of the Focus Issue of Selected Papers from IMLB 2016 with Invited Papers Celebrating 25 Years of Lithium Ion Batteries.*

Over the last decades a progressive miniaturization of electronic components took place. As a result there is an increasing demand for micro-sized power sources that drives the current research on thin film batteries. Possible applications range from sensors and radio-frequency identification tags to implantable medical devices. For these applications an all-solid-state thin film Li-ion battery is desirable due to considerable advantages such as excellent safety properties and easy integration in microelectronics. Furthermore, the energy density of such an all-solid-state cell can be increased compared to a cell with conventional liquid electrolyte, if the chosen solid electrolyte material is stable toward high voltage cathode materials as well as toward a lithium metal anode. The garnet-type solid electrolyte $Li_7La_3Zr_2O_{12}$ (LLZO), first reported in 2007 by Murugan et al.,[1] is a material that combines those properties with reasonably high lithium ion conductivity of up to $2.3 \cdot 10^{-5}$ S · cm^{-1} in its tetragonal[2] and up to $1.2 \cdot 10^{-3}$ S · cm^{-1} in its cubic[3] modification. However, these high conductivity values have so far only been achieved for bulk ceramics, but not for thin films. Apparently, over the last years researchers have focused on the optimization of the lithium ion conductivity in bulk ceramics, e.g. by stabilization of the cubic LLZO phase via doping,[4,5] while only a few publications have addressed LLZO thin film deposition at all.[6–12] The advantage of thin films is that their lithium ion conductivity for the use in an all-solid-state battery does not need to be as high as compared to bulk solid electrolytes, taking into account the electrolyte resistance R:

$$R = l \cdot (\sigma \cdot A)^{-1}, \quad [1]$$

where A is the contact area, l is the thickness and σ is the Li-ion conductivity of the solid electrolyte, respectively. For example, in their recent study Liu et al.[13] report on a functioning bulk all-solid-state battery using cubic LLZO as solid electrolyte with ∼ 1 mm thickness and a Li-ion conductivity of ∼ $7 \cdot 10^{-4}$ S · cm^{-1}.[13] In comparison, under similar conditions and considering the same resistance, this all-solid-state battery could be operated using a solid electrolyte thin film with only ∼1 µm thickness and a Li-ion conductivity of ∼$7 \cdot 10^{-7}$ S · cm^{-1}, according to Eq. 1. Consequently, in case of thin films the lithium ion conductivity of tetragonal LLZO is high enough to be used in an all-solid-state battery, and no stabilization of the cubic LLZO phase is necessary. Therefore, this study concentrates on the optimization of tetragonal LLZO thin film growth.

Up to now, pulsed laser deposition (PLD),[6,8,9] sputtering,[7,14] sol-gel based methods,[10,11] and metal organic chemical vapor deposition (MO-CVD)[12] have been used to deposit LLZO thin films. However, the only report on LLZO thin film fabrication via MO-CVD does not provide any electrochemical characterization of the films. Table I summarizes the reported room temperature lithium ion conductivities of films prepared by different deposition techniques. While undoped and amorphous LLZO thin films exhibit a lithium ion conductivity at room temperature (σ_{RT}) in the order of 10^{-7} S · cm^{-1},[6,7] Al-doped LLZO thin films show a lithium ion conductivity in the range of $10^{-6} - 10^{-5}$ S · cm^{-1}.[8–11] Only one study on cubic LLZO thin films, co-doped with Al and Ta,[14] shows a conductivity value that is comparable to values reported for bulk ceramics. However, this value of $1.2 \cdot 10^{-4}$ S · cm^{-1} is only obtained from an in-plane measurement,[14] while the conductivity measured through the solid electrolyte film is as low as $2.0 \cdot 10^{-9}$ S · cm^{-1}. In conclusion, so far reported lithium ion conductivities of LLZO thin films stay at least one and up to three orders of magnitude below the values reported for bulk ceramics, independent of the deposition technique used. Additionally, the reported activation energies (E_a) vary from as low as 0.18 eV up to 0.70 eV, but the origin for this broad range of E_a remains unclear. Therefore, more research on LLZO thin film deposition is required to gain a better understanding of the processes that lead to such low σ_{RT} and this broad range of E_a compared to bulk ceramics.

Regarding the deposition technique, CVD allows for homogeneous growth of thin films over large areas with high deposition rates and a very high purity.[15] Recently, our group established a

[z]E-mail: cloho@nano.tu-darmstadt.de

Table I. An overview of the reported lithium ion conductivity values of LLZO thin films at room temperature (σ_{RT}). For a better comparison the phase composition, dopant element, deposition technique and activation energy (E_a) are given.

Phase	Dopant	Deposition	σ_{RT} [S · cm^{-1}]	E_a [eV]	Reference
amorphous	no	PLD	$3.35 \cdot 10^{-7}$	0.36	6
amorphous	no	sputtering	$4 \cdot 10^{-7}$	0.70	7
cubic (111)	Al	PLD	$1.0 \cdot 10^{-5}$	0.52	8
cubic (001)	Al	PLD	$2.5 \cdot 10^{-6}$	0.55	8
amorphous	Al	sol-gel	$1.67 \cdot 10^{-6}$	0.18	10
cubic	Al	sol-gel	$2.4 \cdot 10^{-6}$ #	0.52	11
tetragonal & cubic	Al	PLD	$1.61 \cdot 10^{-6}$ *,#	0.35	9
cubic	Al & Ta	sputtering	$1.2 \cdot 10^{-4}$ *	0.47	14
			$2.0 \cdot 10^{-9}$	n.a.	
tetragonal	no	LA-CVD	$4.2 \cdot 10^{-6}$	0.50	This work

*In-plane measurement; All other data are obtained from measurements through the solid electrolyte film.
σ_{RT} is estimated by an extrapolation of the Arrhenius-type plot.

novel CVD precursor delivery system using CO_2-laser flash evaporation of solid precursors, with the striking advantage that the growth of thin films does not depend on the individual vapor pressure of the precursors, which is unique for a CVD process. Details on this novel CO_2-laser assisted chemical vapor deposition (LA-CVD) and structure-property relationships based on the growth of the electrochemically active cathode material $LiCoO_2$ are described elsewhere.[16]

In this paper, LA-CVD of tetragonal LLZO thin films on silicon and platinum substrates together with a detailed characterization of the resulting microstructure, the phase and the element composition, the phase and the element distribution as well as the electrochemical performance are reported. This is the first report on a detailed electrochemical characterization of CVD grown LLZO films, and therefore the objectives of this study are: (i) to demonstrate the potential of LA-CVD for the growth of garnet-type LLZO solid electrolyte thin films, (ii) to optimize the LA-CVD deposition parameters in order to obtain highly dense, crystalline tetragonal LLZO thin films, (iii) to determine the ionic conductivity and activation energy of the tetragonal LLZO grown under optimized synthesis conditions, and (iv) to discuss the potential of tetragonal LLZO films grown by LA-CVD for all-solid-state Li-ion batteries.

Experimental

Thin film deposition.—A detailed description of the LA-CVD experimental setup used for the deposition of thin films in this study can be found elsewhere.[16] The only modification made to the setup described in Loho et al.[16] is that a porous stainless steel microsieve R200 (Tridelta Siperm GmbH) was used in front of the sample holder to achieve a more uniform gas flow and hence deposition. As precursor materials for the LLZO thin film deposition, 2,2,6,6-tetramethyl-3,5-heptanedionato lithium ($LiC_{11}H_{19}O_2$, Alfa Aesar, 98%), lanthanum(III) acetylacetonate hydrate ($La(C_5H_7O_2)_3 \cdot xH_2O$, abcr GmbH, 99.9%) and zirconium(IV) acetylacetonate ($Zr(C_5H_7O_2)_4$, Sigma Aldrich, 98%) were premixed inside an Ar-filled glove box (MBraun GmbH) with O_2- and H_2O-levels <1 ppm. The Li: La: Zr molar ratio in the precursor mixture was set to 10.5: 3: 2. Thereby, $x = 4$ in $La(C_5H_7O_2)_3 \cdot xH_2O$ was used for the calculation based on a preceding thermogravimetric analysis (TGA) of the lanthanum precursor. A lithium excess of 50% was used to compensate for possible loss of lithium during the synthesis at elevated temperatures. The precursors were evaporated with 80 Watt CO_2-laser power. The films were deposited at 873 K, 973 K and 1073 K under a pressure of 5 mbar. Argon (Air Liquide GmbH, 99.999%) was used as a carrier gas for the precursor delivery and oxygen (Air Liquide GmbH, 99.999%) was used as a reaction gas. In order to study the influence of the oxygen partial pressure on the film formation, the flow of argon (oxygen) was set to 1.5 (1.0) standard liters per minute (slm) and 2.3 (0.2) slm, respectively. These conditions correspond to 40% (8%) of oxygen in a total gas flow of 2.5 slm. After a deposition time of 15 min, the CO_2-laser and hence the precursor delivery were switched off. The sample was kept at its deposition temperature for an additional 15 min under the same conditions as used during the deposition, followed by cooling with a rate of 1 K · s^{-1}. The LLZO films were grown on Si(100) wafers (CrysTec GmbH) and Pt-foil (ChemPUR GmbH, 99.99%).

For the reference Li_2PtO_3 film only the 2,2,6,6-tetramethyl-3,5-heptanedionato lithium precursor was deposited on Pt-foil and the film was grown under the following conditions: 973 K, 5 mbar, 1.5 slm argon, 1.0 slm oxygen, without the use of the microsieve.

Material characterization.—*Phase and element composition.—*The relative element composition was determined by energy dispersive X-ray (EDX) analysis using the EDAX Genesis system attached to the scanning electron microscope (SEM), operated at 30 keV with an energy resolution of about 140 eV. The mapped area was in the order of several 1000 μm^2 and the La to Zr ratio was determined from the La *L*- and Zr *L*-lines. No Au coating was used, since the Au- and Zr-lines overlap in EDX.

The phase composition of all deposited films was investigated by X-ray diffraction (XRD). XRD patterns were recorded on a Bruker D8 Advance diffractometer in Bragg-Brentano geometry with a X-ray tube with fine-focusing Cu anode in a 2θ-range from 10° to 80°. No primary beam monochromator was attached. K_β radiation was removed by a Ni filter, but remains present to a very small fraction of the overall beam intensity (<0.1%). A VANTEC detector and a variable divergence slit were used. The total scan time was 162 minutes. The whole 2θ-range was used for Rietveld analysis[17] with the program TOPAS 5.[18] The instrumental intensity distribution for the X-ray data was determined empirically from a fundamental parameters set, using a reference scan of LaB_6 (NIST 660a).[19] The absorption edge resulting from the Ni filter was modeled using the functionality provided in the TOPAS 5 program. For refinement of the peak shape a double Voigt model with a $cos^{-1}(\theta)$ angular dependence for crystallite size and a $tan(\theta)$ angular dependence for microstrain broadening was used. Reflections belonging to the phases of LLZO, La_2O_3 and Li_2PtO_3 were fitted using the Rietveld method, whereas intensities of the reflections belonging to the Pt substrate were modeled by Pawley-type fits. Only lattice parameters, but no positional parameters, were refined for the respective phases. Since a strong correlation of thermal parameters with the background function was observed, the former was fixed to a value of 1 Å^2. The model of March and Dollase was applied to describe intensity changes resulting from texturing of the thin film samples.[20] In this respect several models with different orientations were tested to determine the best fit to the pattern.

Microstructure.—The microstructure of the LLZO thin films grown at 973 K and 40% O_2 were studied using the secondary electron detector of a Philips XL30 FEG SEM, operated at 15 keV.

Phase and element distribution.—The element and phase distribution of the LLZO thin film grown at 973 K and 40% O_2 on Pt was probed by combined time-of-flight secondary ion mass spectrometry (ToF-SIMS) and X-ray photoelectron spectroscopy (XPS) sputter depth profiling. Both analyses were carried out on the very same sample at adjacent positions after the alternating current (AC) impedance spectroscopy (IS) measurements were completed. After completion of the XPS depth profiling the samples were transferred under argon into the ToF-SIMS spectrometer and subsequently analyzed.

ToF-SIMS was performed on a TOF.SIMS5 instrument (ION-TOF GmbH), equipped with a Bi cluster liquid metal primary ion source and a non-linear time of flight analyzer. The Bi source was operated in the "bunched" mode providing 0.7 ns Bi_1^+ ion pulses at 25 keV energy, an analyzed area of 100 μm by 100 μm, and a lateral resolution of approximately 4 μm. Data acquisition and processing were performed using the ION-TOF SurfaceLab 6 software. Negative polarity spectra were calibrated on the C^-, C_2^-, C_3^-, and C_4^- peaks. Sputter depth profiles were performed using a 2 keV Cs^+ ion beam and a raster size of 500 μm by 500 μm with a beam current of 145 nA.

XPS measurements were performed using a K-Alpha+ XPS instrument (Thermo Fisher Scientific). For data acquisition and processing the Thermo Avantage software was used. The samples were analyzed using a micro-focused, monochromated Al K_α X-ray source with 300 μm spot size. The K-Alpha charge compensation system was employed during analysis, using electrons of 8 eV energy and low-energy argon ions to prevent any localized charge buildup. The spectra were fitted with one or more Voigt profiles (binding energy uncertainty: ± 0.2 eV). The analyzer transmission function, Scofield sensitivity factors,[21] and effective attenuation lengths (EALs) for photoelectrons were applied for quantification. EALs were calculated using the standard TPP-2M formalism.[22] All spectra were referenced to the C 1s peak of hydrocarbon at 285.0 eV binding energy and controlled by means of the well-known photoelectron peaks of metallic Cu, Ag, and Au. Sputter depth profiles were performed using an Ar^+ ion beam at 3 keV, 30° angle of incidence, and a 1 mm by 2 mm raster size. The beam current was 2.3 μA.

Electrochemical characterization.—Alternating current impedance spectroscopy (AC-IS) was used for the electrochemical characterization of the LLZO thin film grown at 973 K and 40% O_2 on Pt. Circular Au front contacts with 2 mm in diameter were sputtered on the thin film and the Pt substrate was used as back contact. Consequently, all measurements using a Solartron analytical 1260A impedance/gain-phase analyzer in a frequency range of 1 MHz − 1 Hz were performed through the solid electrolyte film (refer to Fig. 4e). The applied voltage was 50 mV. The thin film sample was loaded into a cryostat (Janis STVP-200-XG), evacuated and purged with helium (Air Liquide GmbH, 99.999%) twice. To avoid the influence of moisture on the electrochemical performance,[23,24] the sample was heated above 373 K inside the cryostat and the AC-IS data were subsequently recorded in a temperature range from 338 K to 298 K in 10 K steps upon cooling. A least squares fit was applied to the data using the software ZView version 3.4b (Scribner Associates). The activation energy was determined from the Arrhenius plot.

Sample handling.—Care has been taken to keep the air exposure time of the thin film samples as short as possible to prevent ageing between different analyses. Therefore, the samples were stored in an Ar-filled glove box (MBraun GmbH) with O_2- and H_2O-levels <0.1 ppm immediately after thin film deposition and after completion of each characterization technique. It was not possible to avoid air exposure during the XRD measurement, before and after sputtering of the Au contacts as well as for loading the sample into the cryostat.

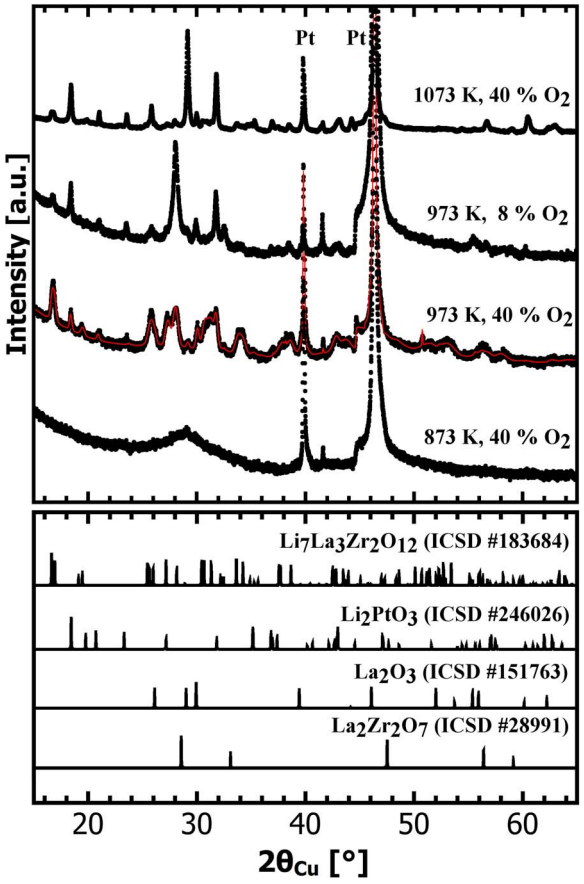

Figure 1. X-ray diffraction patterns (black dots) of LLZO thin films grown by LA-CVD on Pt under various synthesis conditions. While at a deposition temperature of 873 K the obtained film is amorphous, higher deposition temperatures of 973 K and 1073 K lead to crystalline thin films. The Rietveld refinement for optimized growth parameters (973 K and 40% O_2) is plotted as red curve.

Results and Discussion

Phase and element composition.—The XRD patterns of the LLZO thin films grown by LA-CVD under various synthesis conditions on Pt are shown in Fig. 1. Besides the strong intensities of the underlying Pt substrate, the diffraction patterns reveal considerable differences depending on the growth conditions used. While at a deposition temperature of 873 K the film is amorphous, at higher deposition temperatures of 973 K and 1073 K crystalline thin films are obtained. However, only at 973 K and 40% O_2 a polycrystalline garnet-type structure is found as the main phase, confirmed by Rietveld analysis (see Fig. 1 and Table II). Remarkably, even small deviations in synthesis parameters from this sweet spot lead to the formation of mainly undesired phases. Reducing the oxygen partial pressure, i.e. synthesis conditions of 973 K and 8% O_2, results in the formation of a fluorite-type related structure with a lattice parameter of ∼5.51 Å as the main phase. Choosing a higher deposition temperature of 1073 K (40% O_2) leads to the formation of a fluorite-type related structure with a lattice parameter of ∼5.31 Å as the main phase. The pyrochlore-type $La_2Zr_2O_7$, a commonly found impurity phase in the LLZO system, with a pseudo-cubic lattice parameter of ∼5.4 Å is closely related to the observed fluorite-type structure and depending on the detailed La to Zr ratio and their occupation in the structure the lattice parameter varies. The $La_2Zr_2O_7$ phase is well-known to impede the Li-ion movement tremendously and to result in decreased Li-ion conductivity as well as increased activation energy.[9] Consequently, only thin films grown under optimized conditions of 973 K and 40%

Table II. Results obtained from the Rietveld refinement of the XRD data for the LLZO thin film grown at 973 K and 40% O_2, shown in Fig. 1. Numerical errors are given in brackets, but only for the phase quantification and the lattice parameters for the sake of clarity.

		MD-parameter			Lattice parameters		
Phase	wt-%	relative to (hkl)	fraction	Space group	a [Å]	b [Å]	c [Å]
$Li_7La_3Zr_2O_{12}$	85.4(6)	(001) - 1.9	0.9	$14_1/acd$	13.061(2)	-	12.744(2)
		(100) - 1.9	0.1				
Li_2PtO_3	9.6(4)	(111) - 0.3	1.0	C12/m1	5.081(6)	9.028(9)*	5.086(3)
La_2O_3	5.1(4)	-	-	P-3m1	3.930(1)	-	6.130(3)

*The value for the angle beta was refined to 108.50(7)°.

O_2 on Si and Pt will be studied and discussed in detail in the following sections.

By applying the Rietveld method,[17] a quantification of the crystalline phases in the film grown at 973 K and 40% O_2 is achieved. The results are summarized in Table II. Tetragonal $Li_7La_3Zr_2O_{12}$ is present as main phase (85 wt-%), with small amounts of Li_2PtO_3 (10 wt-%) and La_2O_3 (5 wt-%) as secondary phases. The lattice parameters of the LLZO phase agree well with previously reported values of $a = 13.077(1)$ Å and $c = 12.715(4)$ Å for tetragonal LLZO bulk ceramic with 98% relative density.[2]

The Li_2PtO_3 phase is a result of substrate corrosion and it is formed only on the surface of the Pt substrate (see section Phase and element distribution). This corrosion reaction takes place between Li_2CO_3, a decomposition product of the Li-precursor used,[25] and the Pt substrate under oxygen-containing atmosphere. Formation of this compound was already observed in systems other than LLZO deposited by LA-CVD at elevated temperatures.[16] In an earlier study,[16] two ways to suppress the Li_2PtO_3 phase formation in LA-CVD of $LiCoO_2$ were investigated, based on the reaction scheme:

$$Pt + Li_2CO_3 + O_2 \rightarrow Li_2PtO_3 + CO_2. \quad [2]$$

One strategy to suppress the Li_2PtO_3 phase formation was a reduction of the deposition temperature in order to inhibit the kinetics of the corrosion reaction. The second approach was a reduction of the oxygen partial pressure to prevent the oxidation of Pt^0 to Pt^{4+} (Eq. 2). While the first approach was successfully applied in the case of $LiCoO_2$ deposition on Pt by LA-CVD, the second approach showed only a minor effect on the suppression of Li_2PtO_3 phase formation.[16] However, in the case of LLZO deposition none of the two ways to suppress the Li_2PtO_3 phase formation proves to be successful. Lowering the deposition temperature to 873 K inhibits both, the formation of Li_2PtO_3 as well as the formation of crystalline LLZO (see Fig. 1). Reducing the oxygen partial pressure from 40% O_2 to 8% O_2 increases the amount of secondary phases (see Fig. 1), which is most likely due to incomplete decomposition and/or oxidation of the precursor materials.

The small amount of La_2O_3 secondary phase indicates a La-excess in the deposited film originating from the precursor mixture. Since the La-precursor used for the deposition is a hydrate, the amount of water was estimated to be $x = 4$ in $La(C_5H_7O_2)_3 \cdot xH_2O$ based on TGA analysis. However, the degree of hydration may change over time and be different from batch to batch, which could result in a slight lanthanum excess and consequently in small amounts of La_2O_3 secondary phase in the film. EDX analysis of the LLZO thin film deposited on Pt reveals a La to Zr ratio of 1.6, which confirms the slight excess of La. Despite the presence of 5 wt-% of La_2O_3 in the film, a reasonable electrochemical performance is achieved (see section Assignment of the R1-CPE1 element to the $Li_7La_3Zr_2O_{12}$ thin film) indicating that small amounts of La_2O_3 secondary phase are not critical to the impedance analysis.

Rietveld analysis also reveals that the tetragonal LLZO as well as the Li_2PtO_3 phase have a preferred crystallographic orientation. The texture parameters of both phases are refined according to the model of March-Dollase (MD).[20] From the results, given in Table II, it is concluded that the tetragonal $Li_7La_3Zr_2O_{12}$ preferentially grows parallel to (001) and perpendicular to (100) planes, while the Li_2PtO_3 preferentially grows parallel to the (111) plane.

So far, only Tan et al.[6] reported a slightly (100)-textured polycrystalline LLZO film grown on $SrTiO_3$(100) by PLD. No explanation for the textured growth was given,[6] but it could be speculated that it was a substrate driven growth, since the (100)-texture of the LLZO matches the orientation of the $SrTiO_3$(100) single crystal. In the present study, the LLZO films are grown on a rolled, polycrystalline Pt-foil with a strong (002)-texture, as indicated by the (002) reflection of the Pt substrate being highest in intensity (see Fig. 1). Therefore, a correlation with the preferential growth of LLZO parallel to the (001) plane could be assumed. In the study of Kim et al.[8] epitaxial films of cubic LLZO were grown via PLD on $Gd_3Ga_5O_{12}$ single crystal substrates with (001) and (111) orientation, respectively. In-plane conductivities at room temperature were found to differ with values of $2.5 \cdot 10^{-6}$ $S \cdot cm^{-1}$ and $1.0 \cdot 10^{-5}$ $S \cdot cm^{-1}$, which the authors ascribe to differences in strain from epitaxy.[8] Such anisotropic conductivity can also be expected to result from symmetry lowering, e.g. going from a cubic to a tetragonal structure. Since in the present study tetragonal LLZO is grown by LA-CVD, an anisotropic Li-ion conductivity cannot be ruled out, which in addition might be enhanced by film texturing. More experimental as well as theoretical research is needed in this respect, since anisotropy might have a significant impact on the Li-ion conductivity of tetragonal LLZO.

Microstructure.—Micrographs of LLZO thin films deposited at 973 K and 40% O_2 on Si (a, b) as well as on Pt (c, d) are shown in Fig. 2. A dense and homogeneous film growth is observed. The surface roughness of the LLZO film on Si appears to be lower compared to the one on Pt, which is ascribed to the difference in surface roughness of the substrates used, i.e. the Si(100) wafer is polished while the Pt-foil is rolled. Nevertheless, the surface of the LLZO thin film deposited on Pt can be considered as smooth and uniform based on the micrographs (c) and (d) in Fig. 2. The cross-section image (Fig. 2a) clearly reveals the highly dense and regular nature of the thin film. Despite the fact that the density cannot be quantified via SEM, a comparison of the cross-section image (Fig. 2a) with SEM images of sintered LLZO pellets with reported densities above 90%[26–29] confirms the highly dense nature of the LA-CVD grown LLZO film. A film thickness of around 850 nm is estimated from this cross-section for the deposition on Si. Although the growth conditions and therefore the growth rate of LLZO on Si and Pt might slightly vary, a film thickness of similar order of magnitude can be expected for the deposition on Pt. LLZO deposition on Si leads to microcrack formation (Fig. 2b), while the LLZO thin film grown on Pt is free of cracks (Fig. 2d). The reason for the different behavior remains unclear, however, it is possible that the lattice strain induced by the relatively high cooling rate of about 1 $K \cdot s^{-1}$ is accommodated easier by the polycrystalline Pt-foil than by the Si(100) single crystal. Another remarkable feature of the LLZO film on Pt is the very homogeneous growth over a large area of several mm^2 (Fig. 2c). Such a highly dense and homogeneous microstructure is important for the reliability of the AC-IS measurements, since a large front contact with 2 mm in diameter is used in this study.

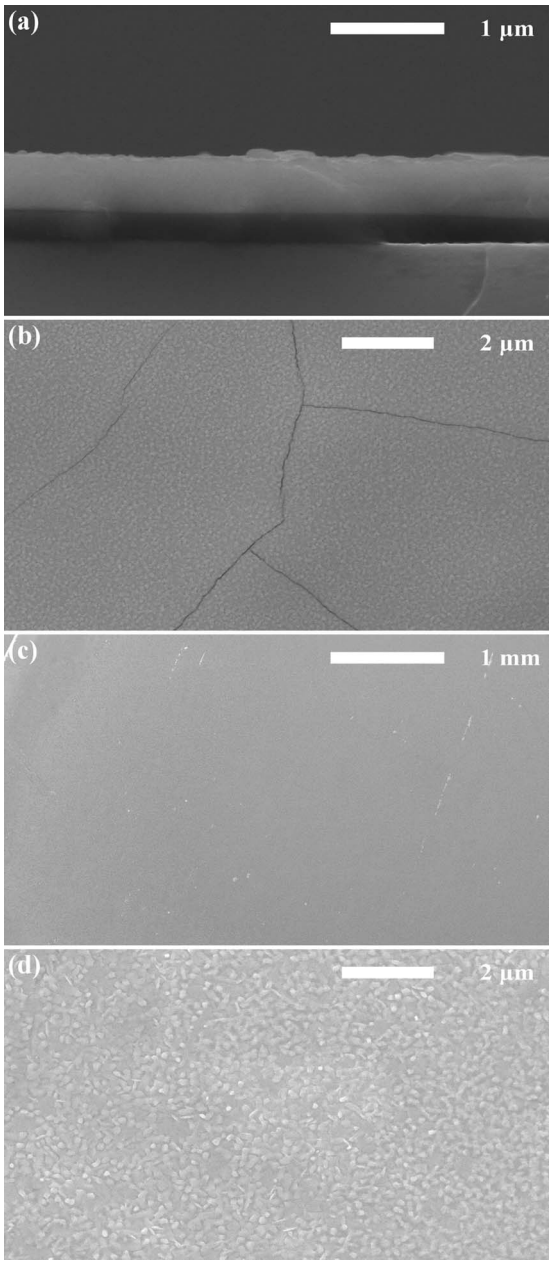

Figure 2. Secondary electron micrographs of LLZO thin films deposited at 973 K and 40% O_2 on Si (a, b) and Pt (c, d). Image (a) shows the LLZO cross-section and images (b), (c), (d) show the top view. A dense and homogeneous film growth is observed under the deposition conditions used. Microcrack formation is only observed for LLZO films deposited on Si (b).

Additionally, it is a mandatory requirement for the application in an all-solid-state thin film Li-ion battery in order to avoid a short circuit due to pinholes and to allow for the use of a very thin solid electrolyte layer.

Phase and element distribution.—In order to correlate the findings described in this section with the electrochemical performance (section Electrochemical properties) of the LLZO thin film, the location of the ToF-SIMS and XPS measurements was chosen to be on the Au contact, where the electrochemical characterization has taken place.

The ToF-SIMS sputter depth profile (Fig. 3a) illustrates qualitatively the development of selected chemical groups, while the XPS sputter depth profile (Fig. 3b) provides quantitative information on the element distribution dependent on sputter time. The following results are obtained: (1) At around 450 s in ToF-SIMS the simultaneous increase in Li^- and CO_3^- signals provides clear evidence of Li_2CO_3 being present at the interface Au | LLZO. This finding is supported by the development of the C 1s signal in the XPS profile. Since care has been taken to keep the air exposure time of the sample as short as possible (see section Sample handling), this result implies that the Li_2CO_3 formation at the surface of the LLZO film takes place within only a few hours of air exposure. (2) The LaO^- and ZrO^- signals in ToF-SIMS as well as the Zr 3d and La 3d signals in XPS appear and vanish simultaneously and run approximately in parallel to each other over the entire sputter time, suggesting a very homogeneous element distribution. (3) For XPS sputter times from 1550 s to 3050 s, the La to Zr ratio is calculated from the XPS data to be 1.5 on average, which corresponds to the desired composition of tetragonal $Li_7La_3Zr_2O_{12}$. (4) For XPS sputter times from 800 s to 1550 s, the La to Zr ratio is slightly higher than 1.5. A possible reason could be that the small amount of La_2O_3 secondary phase found in XRD is located at the film surface. (5) The LLZO film is free of carbon, which can be seen by the disappearance of the C 1s signal for XPS sputter times above 1000 s. (6) The Li_2PtO_3 phase found in XRD is located only at the interface LLZO | Pt, which is concluded from the simultaneous onset of PtO^- and Pt^- signal at about 3300 s in ToF-SIMS. This finding strongly supports the substrate corrosion mechanism (Eq. 2), which was assumed in section Phase and element composition. The fact that Li_2PtO_3 only appears at the interface LLZO | Pt is very important for the interpretation of the AC-IS data (section Electrochemical properties), because it allows to treat the LLZO film and Li_2PtO_3 interface layer as series electrical connection.

Unfortunately, reliable quantification of Li throughout the entire XPS sputter profile could not be achieved, resulting from a strong overlap of the Au $5p_{1/2}$, Zr 4s and Pt $5p_{3/2}$ with the Li 1s signal (see Fig. 3c).

Electrochemical properties.—Nyquist plots (Fig. 4a and 4b) of the AC-IS data measured through the LLZO thin film (Fig. 4e), grown under optimized conditions, show two strongly superimposed semicircles at high and intermediate frequencies together with a low frequency tail. The latter results from Li-ion blocking at the electrodes and demonstrates that the material under investigation is a Li-ion conductor, with very low partial electronic conductivity.[30] The two superimposed semicircles observed in the Nyquist plots become more evident in a Bode-type plot (Fig. 4c), namely as two minima in the phase shift curve. They are characteristic for a series of two R-CPE elements, where *R* is an ohmic resistance and *CPE* is a constant phase element. Therefore, the equivalent circuit model shown in Fig. 4d is applied for data analysis. In total 4 electrical elements: R0, R1-CPE1, R2-CPE2 and CPE3, connected in series are used to describe the impedance spectrum. The fit results for R1-CPE1 and R2-CPE2 are summarized in Table III. Combining these fit results with the results on the phase and element composition (section Phase and element composition) as well as the phase and element distribution (section Phase and element distribution) leads to the following assignment of the 4 electrical elements: R0 − contact resistance of the setup (cables, etc.), R1-CPE1 − LLZO solid electrolyte, R2-CPE2 − Li_2PtO_3 interface layer, CPE3 − low frequency diffusion. In order to verify the proposed assignment, in the following subsections, the fit results are discussed and scrutinized in detail.

*Assignment of the R1-CPE1 element to the $Li_7La_3Zr_2O_{12}$ thin film.—*From the fit results for the R1-CPE1 element the total lithium ion conductivity of the LLZO solid electrolyte thin film can be calculated using Eq. 1. The total Li-ion conductivity of the LA-CVD grown LLZO thin film at 298 K is found to be $4.2 \cdot 10^{-6}$ $S \cdot cm^{-1}$. From the Arrhenius plot (Fig. 5) the activation energy of the charge transport in the LLZO film can be estimated to be 0.50 eV. Compared to bulk ceramics, the presented Li-ion conductivity and activation energy of the LLZO thin film grown by LA-CVD agree well with values

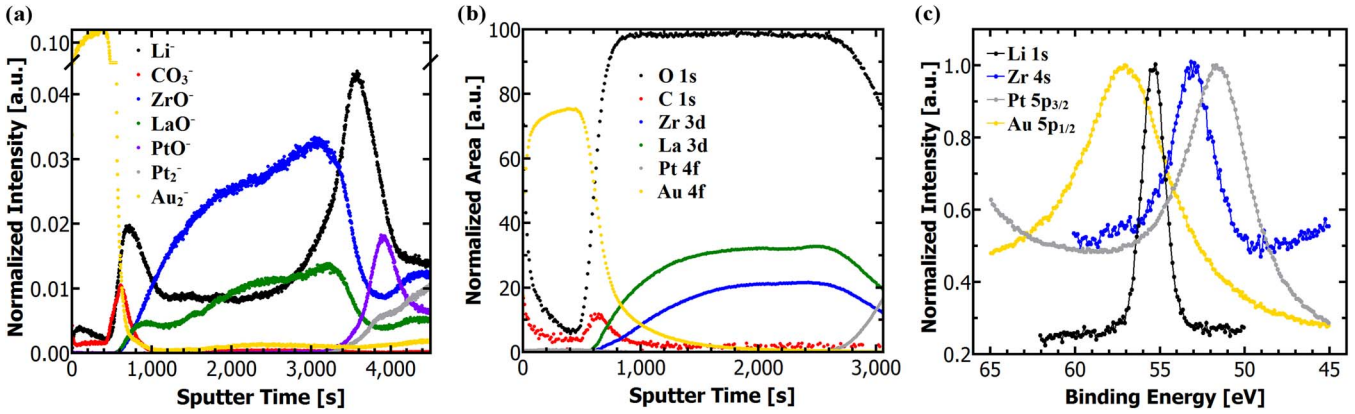

Figure 3. ToF-SIMS (a) and XPS (b) sputter depth profiles of the LLZO thin film grown at 973 K and 40% O_2 on Pt. Please note that the *y*-axis in (a) is interrupted from 0.045 to 0.085 for the sake of clarity. (c) XPS binding energy region of Li 1s to illustrate the strong overlap of the Au $5p_{1/2}$, Zr 4s and Pt $5p_{3/2}$ with the Li 1s signal. The solid lines are only a guide to the eye.

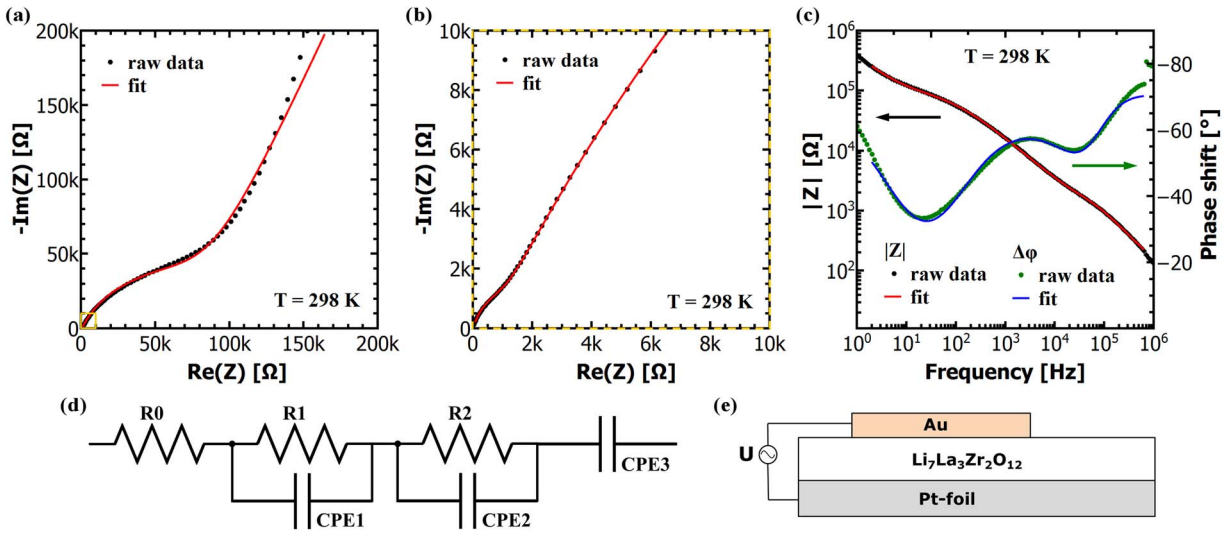

Figure 4. Impedance spectroscopy data taken at 298 K for the LLZO thin film grown at 973 K and 40% O_2 on Pt: (a) Nyquist plot, (b) a close-up of the frequency region from 1 MHz to 2 kHz (yellow square in (a)), (c) Bode plot, (d) equivalent circuit used for the fit, and (e) illustration of the measurement geometry. Raw data of the impedance and phase shift are shown as black and green dots, respectively, whereas the fit to the impedance and phase shift are plotted as red and blue lines, respectively.

reported for tetragonal LLZO, which range from $3.1 \cdot 10^{-7}$ S · cm^{-1} (0.67 eV)[31] and $1.2 \cdot 10^{-6}$ S · cm^{-1} (0.55 eV)[32] to $2.3 \cdot 10^{-5}$ S · cm^{-1} (0.41 eV).[2] Strong differences in the reported Li-ion conductivities as well as the activation energies are often assigned to the use of different synthesis techniques and compaction methods that can result in ceramics with different microstructures and densities. Especially the overall density is known to play a crucial role for obtaining high conductivities. Considerable effort has been made to achieve higher densities for bulk ceramics using nano-grained LLZO,[26] field assisted sintering technique for compaction,[27,28] or sintering aids like Ga.[29] Therefore, the fact that the performance of the tetragonal LLZO thin film grown by LA-CVD is among the best values reported for tetragonal LLZO so far, is attributed primarily to the high density of the film (see Fig. 2). Further properties of the LA-CVD grown LLZO film that might contribute to the good performance are the high purity of the film being free of carbon as well as Li-ion blocking $La_2Zr_2O_7$ phase and its high crystallinity (see Fig. 1). The latter becomes apparent in comparison to the films with an amorphous structure, where low

Table III. Summary of the fit results of the AC-IS data in the temperature range from 338 K to 298 K. Capacitance values, *C1* and *C2*, are calculated according to Eq. 3. X^2 is the square of the standard deviation between the original and the calculated spectrum.

T [K]	R1 [kΩ]	CPE1 [nFs$^{(\varphi 1-1)}$]	φ1 [1]	C1 [nF]	R2 [kΩ]	CPE2 [nFs$^{(\varphi 2-1)}$]	φ2 [1]	C2 [nF]	X^2 [10^{-4}]
298	0.64	5.2	1.0*	5.2	79	117	0.76	27	3
308	0.30	7.2	0.97	5.0	28	148	0.76	27	1
318	0.17	14	0.92	4.4	12	172	0.76	24	2
328	0.10	41	0.85	4.4	4.5	175	0.78	22	3
338	0.06	581	0.67	4.1	2.1	219	0.77	21	2

*During the fit φ1 was fixed to 1.0, because the fit routine gave an unphysical value of 1.05.

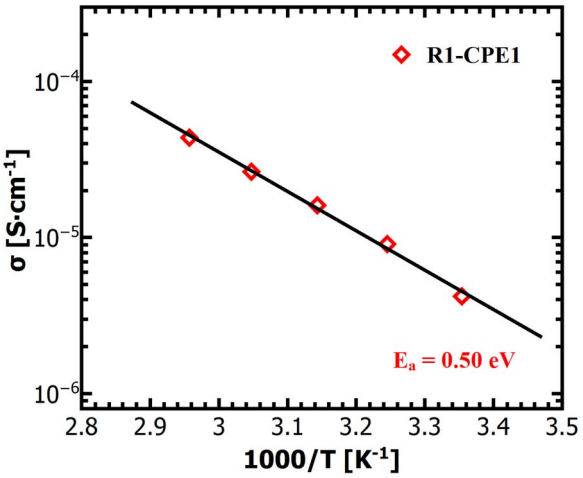

Figure 5. Arrhenius plot in the temperature range from 338 K to 298 K for the R1-CPE1 element, which is assigned to the total Li-ion conductivity of the LLZO film. An exponential fit (black line) is applied to the data (red rhombs). The activation energy is determined from the slope of the fit.

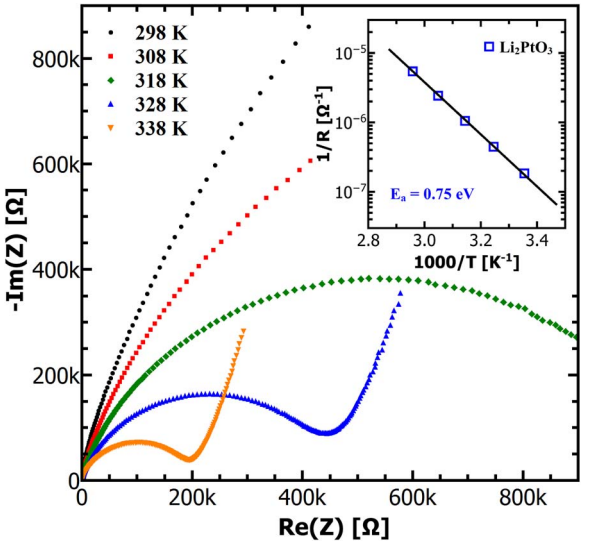

Figure 6. Nyquist plot in the temperature range from 338 K to 298 K for the reference Li_2PtO_3 film. One intermediate frequency semicircle and a low frequency tail are observed. Inset: Arrhenius plot of the reference Li_2PtO_3 film. Please note that 1/*R* instead of σ is plotted on the *y*-axis, since the film thickness could not be determined.

Li-ion conductivities are observed (see Table I). It is noteworthy that all these favorable characteristics are obtained at a deposition temperature as low as 973 K, demonstrating the strength and the capability of LA-CVD in the growth of garnet-type LLZO solid electrolyte films.

In order to justify the proposed assignment of the R1-CPE1 element to the total (bulk + grain boundary) Li-ion conductivity of the LLZO film, the capacitance *C* (listed in Table III) can be calculated from the fit parameters of *R*, *CPE* and the exponential factor φ according to:[33]

$$C = \left(CPE \cdot R^{1-\varphi}\right)^{1/\varphi} \quad [3]$$

For the high frequency arc, capacitances *C1* of about 5 nF are obtained. According to literature,[34] and taking into account the cell constant ($l/A = 2.7 \cdot 10^{-3}$ cm^{-1}) used in this study as well as a typical relative permittivity (ε_r ~50) for LLZO,[35] bulk and grain boundary effects (as responsible phenomena for the impedance spectrum) are expected to have capacitances of 1.6 nF and 16 nF - 16 μF, respectively. The observed capacitances *C1* are slightly higher than the capacitance expected for only bulk Li-ion conduction, and much lower than the range of capacitances expected for only grain boundary Li-ion conduction. The wide range of grain boundary capacitance is due to its strong dependence on the microstructure, i.e. poorly sintered materials show lower capacitance while well sintered materials show higher capacitance.[34]

Based on the secondary electron micrographs (Fig. 2) it is assumed that the LLZO film grown at 973 K is well sintered, hence the capacitance *C1* of the high frequency arc is most likely to be bulk dominated. Another approach to test the validity of the proposed assignment is to calculate the relative permittivity, ε_r, from Eq. 4:

$$\varepsilon_r = (C \cdot l) \cdot (A \cdot \varepsilon_0)^{-1}. \quad [4]$$

The constant ε_0 is the vacuum permittivity. For a capacitance of 5 nF a relative permittivity of 152 is calculated, which is about 3 times the value previously reported for bulk transport of Li-ions in Mo-doped LLZO bulk ceramics.[35] It is known that the calculation of ε_r on the basis of a simple parallel-plate capacitor (Eq. 4) leads to values higher than expected, if bulk and grain boundary conduction are of similar order of magnitude.[36] Consequently, the deviation of ε_r toward higher values indicates a small grain boundary contribution to the R1-CPE1 element. In summary, an unambiguous assignment of the R1-CPE1 element to only bulk Li-ion conduction is not possible in the present study, hence it is assigned to the total Li-ion conductivity of the LLZO film.

Assignment of the R2-CPE2 element to the Li_2PtO_3 interface layer.—The calculation of the capacitance *C2* from the fit results based on Eq. 3 leads to a value of 27 nF, which is less than one order of magnitude higher than *C1* and at the lower end of capacitance values expected for grain boundary effects (see section Assignment of the R1-CPE1 element to the $Li_7La_3Zr_2O_{12}$ thin film). Thus, it could be argued that the intermediate frequency semicircle in the impedance spectrum is due to grain boundary conduction in the LLZO and not as earlier proposed in this section due to the Li_2PtO_3 interface layer. In order to rule this out and to clarify that the intermediate frequency arc arises from the Li_2PtO_3 interface, the activation energy of the R2-CPE2 element is estimated to be 0.79 eV from the temperature dependent AC-IS data. This value is much higher than previously reported values for activation energies in tetragonal LLZO as discussed in section Assignment of the R1-CPE1 element to the $Li_7La_3Zr_2O_{12}$ thin film. High activation energies in the LLZO system are often related to low relative densities,[2] but this can be ruled out in the present study since very dense thin films are grown (see Fig. 2). Therefore, based on the high activation energy it is more likely that the R2-CPE2 element originates from the Li_2PtO_3 interface layer. In fact, O'Malley et al.[37] reported the activation energy of Li_2PtO_3 to be 0.92 eV, being almost twice the value of 0.49 eV previously reported by Okada et al.,[38] although both studies used a polycrystalline Li_2PtO_3 pellet with 63% theoretical density. Because both reported values deviate strongly from each other, and in order to come to a final conclusion, a reference Li_2PtO_3 film was grown by LA-CVD on Pt under similar conditions as used for LLZO. This reference Li_2PtO_3 film was analyzed by AC-IS in the same manner as the LLZO film. The Nyquist plot (Fig. 6) shows one intermediate frequency semicircle and a low frequency tail that correspond to the R2-CPE2 and CPE3 element of the LLZO impedance spectrum, respectively. From the Arrhenius plot (inset in Fig. 6) the activation energy is determined to 0.75 eV for the reference Li_2PtO_3 film. The estimated activation energy of the R2-CPE2 element (0.79 eV, obtained from the LLZO impedance data) resembles the one of the reference Li_2PtO_3 film and consequently validates the proposed assignment of the R2-CPE2 element to the Li_2PtO_3 interface layer.

Potential of LA-CVD grown LLZO thin films for all-solid-state Li-ion batteries.—In case of bulk-type all-solid-state batteries a Li-ion conductivity of the solid electrolyte material that comes close to

values obtained for commercial liquid electrolytes (about 10^{-2} - 10^{-3} $S \cdot cm^{-1}$) is desirable in order to achieve a low internal resistance of the battery (refer to Eq. 1). However, in case of thin film solid electrolytes the decrease in thickness down to some hundreds of nanometers allows for the use of materials with lower ionic conductivity as pointed out in the introduction. A prominent example is amorphous lithium phosphorus oxynitride (LiPON), with a room temperature Li-ion conductivity of $2 \cdot 10^{-6}$ $S \cdot cm^{-1}$,[39] which is most frequently employed in current all-solid-state thin film Li-ion batteries.[40] In comparison to LiPON, the tetragonal LLZO thin film grown by LA-CVD in this study shows a higher room temperature Li-ion conductivity of $4.2 \cdot 10^{-6}$ $S \cdot cm^{-1}$ and accordingly, from a conductivity point of view, should also be applicable for the use in all-solid-state thin film Li-ion batteries like LiPON.

In an earlier study, the growth of $LiCoO_2$ thin films by LA-CVD for the use as cathode material in Li-ion batteries has been shown to be successful.[16] Together with the results on LLZO solid electrolyte thin film deposition presented in this study, an all-solid-state thin film Li-ion battery by LA-CVD comes into reach, growing LLZO and $LiCoO_2$ films on top of each other. Such an exclusive LA-CVD battery concept could either make use of an in-situ plated Li anode,[41] or employ a simple metal oxide (e.g. nickel- or cobalt oxide) thin film anode. The latter would have the advantage that the LLZO solid electrolyte film was sandwiched between the cathode and the anode layer and therefore could be further processed under ambient conditions without degradation. Additionally, if the LLZO was deposited on top of $LiCoO_2$, the Li_2PtO_3 formation could be suppressed (refer to section Phase and element composition). This is of great importance to obtain a functioning all-solid-state battery, because of the large impedance that even a thin Li_2PtO_3 interface layer was shown to have (sections Assignment of the R1-CPE1 element to the $Li_7La_3Zr_2O_{12}$ thin film and Assignment of the R2-CPE2 element to the Li_2PtO_3 interface layer). A further advantage of an all-solid-state thin film Li-ion battery concept by exclusively LA-CVD would be the realization of a 3D-microbattery design due to the capability of CVD to conformal deposition. This would result in an additional increase of the area specific energy density and ensure a high power capability for the 3D-microbattery cell.[40]

Our final remark is about the potential of using CVD in industrial battery fabrication processes. In the fields of semiconductor and nanotechnology industries, CVD in various configurations such as MO-CVD, plasma enhanced (PE) CVD and low pressure (LP) CVD are matured techniques since many years. Our novel CO_2-laser assisted chemical vapor deposition has the striking advantage that the film growth does not depend on the individual vapor pressure of the solid precursors, which is unique for a CVD process. This simplifies the precursor delivery tremendously and allows for the controlled growth of high quality multicomponent films with a dense and homogeneous microstructure, free of cracks. Also, the grown films show a homogeneous element distribution and are free of carbon as shown in this study by means of Li-ion conducting LLZO solid electrolyte. Therefore, we believe that the LA-CVD technique might be suited for industrial battery fabrication.

Conclusions

This study demonstrates the successful growth of garnet-type Li-ion conducting $Li_7La_3Zr_2O_{12}$ solid electrolyte thin films by a novel CO_2-laser assisted chemical vapor deposition technique. In addition to a detailed characterization of the microstructure of the LLZO films, their phase and element composition as well as their phase and element distribution, this report provides the first electrochemical characterization of CVD grown LLZO. We show that the deposition temperature and the oxygen partial pressure are crucial process parameters to obtain high quality, well performing tetragonal LLZO thin films. Under optimum growth conditions (973 K and 40% O_2), highly dense and homogeneous LLZO thin films free of cracks are grown on Pt. Phase quantification by means of Rietveld analysis shows that the grown film consists of tetragonal LLZO mainly (85 wt-%), with small amounts of Li_2PtO_3 (10 wt-%) and La_2O_3 (5 wt-%) as secondary phases. Furthermore, a preferred orientation is determined for the polycrystalline LLZO as well as the Li_2PtO_3 phase. A combined analysis using ToF-SIMS and XPS sputter depth profiling proves that the Li_2PtO_3 is only present at the interface between LLZO and Pt, which is essential for the interpretation of the AC-IS data, as it allows to treat the LLZO film and the Li_2PtO_3 interface layer as series electrical connection. Moreover, a thin layer of Li_2CO_3 is found exclusively at the surface of the LLZO film and apart from that the deposited thin films are free of carbon.

Two contributions to the AC-IS spectrum are identified and clearly assigned to the LLZO solid electrolyte thin film and the Li_2PtO_3 interface layer, based on experimental results and numerical considerations. A total ionic conductivity of $4.2 \cdot 10^{-6}$ $S \cdot cm^{-1}$ at 298 K with an activation energy of 0.50 eV is found for the tetragonal LLZO thin film grown by LA-CVD. These results are in good agreement with values obtained from bulk ceramic studies. Furthermore, this is the highest conductivity value reported for tetragonal LLZO thin films so far, being about one order of magnitude higher than previously reported values for tetragonal LLZO thin films prepared by sputtering and pulsed laser deposition. The high ionic conductivity together with the dense and homogeneous microstructure free of cracks make LA-CVD grown LLZO films interesting candidates for the use in all-solid-state (thin film) lithium ion batteries, with the potential of using CVD in industrial battery fabrication processes.

Acknowledgments

The authors gratefully acknowledge a major equipment grant "Competence South – Electrochemistry for Electromobility" from the Federal Ministry of Education and Research (contract no. 6091/89161/03KP801). Further support for an equipment grant by the State of Hesse is appreciated. CL, RD and HH acknowledge the financial support by the Portfolio project "Electrochemical storage in systems" provided by Helmholtz Association. OC gratefully acknowledges support from the German Research Foundation within an Emmy Noether Research Fellowship (grant no. CL551/2-1). The XPS instrument was supported by the Federal Ministry of Economics and Technology on the basis of a decision by the German Bundestag. Special thanks go to Geoffrey M. Tan (TU Darmstadt, Germany) for technical support, and Daniel Rettenwander (U Salzburg, Austria), Andreas Welzl and Jürgen Fleig (TU Wien, Austria) for fruitful discussions.

References

1. R. Murugan, V. Thangadurai, and W. Weppner, *Angew. Chem. Int. Ed. Engl.*, **46**, 7778 (2007).
2. J. Wolfenstine, E. Rangasamy, J. L. Allen, and J. Sakamoto, *J. Power Sources*, **208**, 193 (2012).
3. D. Rettenwander, G. Redhammer, F. Preishuber-Pflügl, L. Cheng, L. Miara, R. Wagner, A. Welzl, E. Suard, M. M. Doeff, M. Wilkening, J. Fleig, and G. Amthauer, *Chem. Mater.*, **28**, 2384 (2016).
4. Y. Ren, K. Chen, R. Chen, T. Liu, Y. Zhang, and C.-W. Nan, *J. Am. Ceram. Soc.*, **98**, 3603 (2015).
5. V. Thangadurai, S. Narayanan, and D. Pinzaru, *Chem. Soc. Rev.*, **43**, 4714 (2014).
6. J. Tan and A. Tiwari, *ECS Solid State Lett.*, **1**, Q57 (2012).
7. D. J. Kalita, S. H. Lee, K. S. Lee, D. H. Ko, and Y. S. Yoon, *Solid State Ionics*, **229**, 14 (2012).
8. S. Kim, M. Hirayama, S. Taminato, and R. Kanno, *Dalton Trans.*, **42**, 13112 (2013).
9. J. S. Park, L. Cheng, V. Zorba, A. Mehta, J. Cabana, G. Chen, M. M. Doeff, T. J. Richardson, J. H. Park, J. Son, and W. Hong, *Thin Solid Films*, **576**, 55 (2015).
10. R. Chen, M. Huang, W. Huang, Y. Shen, Y. Lin, and C. Nan, *J. Mater. Chem. A*, **2**, 13277 (2014).
11. K. Tadanaga, H. Egawa, A. Hayashi, M. Tatsumisago, J. Mosa, M. Aparicio, and A. Duran, *J. Power Sources*, **273**, 844 (2015).
12. H. Katsui and T. Goto, *Thin Solid Films*, **584**, 130 (2015).
13. T. Liu, Y. Ren, Y. Shen, S. Zhao, Y. Lin, and C. Nan, *J. Power Sources*, **324**, 349 (2016).
14. S. Lobe, C. Dellen, M. Finsterbusch, H.-G. Gehrke, D. Sebold, C.-L. Tsai, S. Uhlenbruck, and O. Guillon, *J. Power Sources*, **307**, 684 (2016).
15. M. L. Hitchman and K. F. Jensen, *Chemical vapor deposition: Principles and applications*, Academic Press, London, (1993).

16. C. Loho, A. J. Darbandi, R. Djenadic, O. Clemens, and H. Hahn, *Chem. Vap. Depos.*, **20**, 152 (2014).
17. H. M. Rietveld, *J. Appl. Crystallogr.*, **2**, 65 (1969).
18. Topas V5 User's Manual, *General profile and structure analysis software for powder diffraction data*, Bruker AXS, Karlsruhe (2014).
19. R. W. Cheary, A. A. Coelho, and J. P. Cline, *J. Res. Natl. Inst. Stand. Technol.*, **109**, 1 (2004).
20. W. A. Dollase, *J. Appl. Crystallogr.*, **19**, 267 (1986).
21. J. H. Scofield, *J. Electron Spectros. Relat. Phenomena*, **8**, 129 (1976).
22. S. Tanuma, C. J. Powell, and D. R. Penn, *Surf. Interface Anal.*, **21**, 165 (1994).
23. Y. Jin and P. J. McGinn, *J. Power Sources*, **239**, 326 (2013).
24. G. Larraz, A. Orera, and M. L. Sanjuán, *J. Mater. Chem. A*, **1**, 11419 (2013).
25. P. Fragnaud, R. Nagarajan, D. M. Schleich, and D. Vujic, *J. Power Sources*, **54**, 362 (1995).
26. J. Sakamoto, E. Rangasamy, H. Kim, Y. Kim, and J. Wolfenstine, *Nanotechnology*, **24**, 424005 (2013).
27. M. Botros, R. Djenadic, O. Clemens, M. Möller, and H. Hahn, *J. Power Sources*, **309**, 108 (2016).
28. Y. Zhang, F. Chen, R. Tu, Q. Shen, and L. Zhang, *J. Power Sources*, **268**, 960 (2014).
29. H. El Shinawi and J. Janek, *J. Power Sources*, **225**, 13 (2013).
30. V. Thangadurai, R. A. Huggins, and W. Weppner, *J. Power Sources*, **108**, 64 (2002).
31. I. Kokal, M. Somer, P. H. L. Notten, and H. T. Hintzen, *Solid State Ionics*, **185**, 42 (2011).
32. R. Djenadic, M. Botros, C. Benel, O. Clemens, S. Indris, A. Choudhary, T. Bergfeldt, and H. Hahn, *Solid State Ionics*, **263**, 49 (2014).
33. A. Lasia, *Electrochemical impedance spectroscopy and its applications*, Springer New York, New York (2014).
34. J. T. S. Irvine, D. C. Sinclair, and A. R. West, *Adv. Mater.*, **2**, 132 (1990).
35. D. Rettenwander, A. Welzl, L. Cheng, J. Fleig, M. Musso, E. Suard, M. M. Doeff, G. J. Redhammer, and G. Amthauer, *Inorg. Chem.*, **54**, 10440 (2015).
36. W. I. Archer and R. D. Armstrong, in *Electrochemistry: Volume* 7, H. R. Thirsk, Editor, p. 157, The Royal Society of Chemistry (1980).
37. M. J. O'Malley, H. Verweij, and P. M. Woodward, *J. Solid State Chem.*, **181**, 1803 (2008).
38. S. Okada, J. Yamaki, K. Asakura, H. Ohtsuka, H. Arai, S. Tobishima, and Y. Sakurai, *Electrochim. Acta*, **45**, 329 (1999).
39. J. B. Bates, N. J. Dudney, G. R. Gruzalski, R. A. Zuhr, A. Choudhury, C. F. Luck, and J. D. Robertson, *Solid State Ionics*, **53**, 647 (1992).
40. J. F. M. Oudenhoven, L. Baggetto, and P. H. L. Notten, *Adv. Energy Mater.*, **1**, 10 (2011).
41. B. J. Neudecker, N. J. Dudney, and J. B. Bates, *J. Electrochem. Soc.*, **147**, 517 (2000).